



Upscaling Sediment-Flux-Dependent Fluvial Bedrock Incision to Long Timescales

Jens M. Turowski¹
¹German Research Centre for Geosciences GFZ, Helmholtzzentrum Potsdam, Potsdam, Germany

Key Points:

- Analytical solution from explicit upscaling of a sediment-flux-dependent fluvial bedrock incision model to long time scales
- The model includes solutions similar to those obtained in the stream power paradigm, in addition to other possible solutions
- The model explicitly resolves forcing behavior and highlights potential dynamic feedbacks that have so far not been considered

Correspondence to:

J. M. Turowski,
turowski@gfz-potsdam.de

Citation:

Turowski, J. M. (2021). Upscaling sediment-flux-dependent fluvial bedrock incision to long timescales. *Journal of Geophysical Research: Earth Surface*, 126, e2020JF005880. <https://doi.org/10.1029/2020JF005880>

Received 15 SEP 2020

Accepted 22 FEB 2021

Abstract Fluvial bedrock incision is driven by the impact of moving bedload particles. Mechanistic, sediment-flux-dependent incision models have been proposed, but the stream power incision model (SPIM) is frequently used to model landscape evolution over large spatial and temporal scales. This disconnect between the mechanistic understanding of fluvial bedrock incision on the process scale, and the way it is modeled on long time scales presents one of the current challenges in quantitative geomorphology. Here, a mechanistic model of fluvial bedrock incision that is rooted in current process understanding is explicitly upscaled to long time scales by integrating over the distribution of discharge. The model predicts a channel long profile form equivalent to the one yielded by the SPIM, but explicitly resolves the effects of channel width, cross-sectional shape, bedrock erodibility, and discharge variability. The channel long profile chiefly depends on the mechanics of bedload transport, rather than bedrock incision. In addition to the imposed boundary conditions specifying the upstream supply of water and sediment, and the incision rate, the model includes four free parameters, describing the at-a-station hydraulic geometry of channel width, the dependence of bedload transport capacity on channel width, the threshold discharge of bedload motion, and reach-scale cover dynamics. For certain parameter combinations, no solutions exist. However, by adjusting the free parameters, one or several solutions can usually be found. The controls on and the feedbacks between the free parameters have so far been little studied, but may exert important controls on bedrock channel morphology and dynamics.

Plain Language Summary Bedrock erosion by rivers is driven by the impact of moving sediment particles, chipping away tiny pieces of rocks in their passage. Sediment transport occurs infrequently, during floods. Over thousands of years, this slow process shapes the river, sometimes leading to the creation of spectacular landforms such as gorges. Mechanistic models of fluvial bedrock erosion explicitly take into account the effects of moving sediment particles, while models used for long time scales do not. Here, the connection between mechanistic and long-term models is made explicit by integrating a mechanistic model over the entire distribution of floods, yielding solutions for the long-term erosion rate and the channel bed slope. Some of these solutions are similar to those used previously, but other solutions are also possible, showing the rich dynamic behavior that rivers can exhibit. The solutions make explicit the role of lithology, channel width, and discharge variability, which were previously hidden in a single lumped calibration parameter.

1. Introduction

River processes are driven by flowing water. Water discharge varies over time, according to the spatial and temporal patterns of precipitation in the catchment, its size, and its hydrological properties (e.g., Deal et al., 2018). While rivers may respond to this variability by visibly changing their shape over the course of a single flood event, over long time scales, it is thought that fluvial incision rates and average river morphology depend on some characteristic statistics of the distribution of discharge (e.g., Blom et al., 2017; DiBiase & Whipple, 2011; Lague et al., 2005; Molnar, 2001; Molnar et al., 2006; Scherler et al., 2017; Tucker, 2004). Describing the relationship between short-term mechanistic processes active in rivers and the long-term evolution of river morphology is a central problem in fluvial morphology, both for operational challenges such as river training and management, and for the understanding of the evolution of landforms over geological timescales.

Bedrock rivers are a key component of erosional landscapes such as active mountain belts. On the process scale, fluvial bedrock incision is thought to be driven by the impact of moving bedload particles. Numerous

© 2021. The Authors.

This is an open access article under the terms of the [Creative Commons Attribution-NonCommercial License](#), which permits use, distribution and reproduction in any medium, provided the original work is properly cited and is not used for commercial purposes.

observations from laboratory experiments and natural streams have by now been reported, demonstrating that bedload transport exerts a dominant control on the patterns and rates of erosion (e.g., Beer et al., 2017; Finnegan et al., 2007; Mishra et al., 2018; Shepherd, 1972; Turowski, Hovius, Hsieh, et al., 2008; Wohl & Ikeda, 1997). A number of sediment-related effects have been identified (e.g., Sklar & Dietrich, 2001; Turowski et al., 2013), two of which seem to be most important. The tools effect arises because fluvial bedrock erosion is driven by the impacts of moving bedload particles, implying that an increasing number of moving particles leads to an increasing number of impacts and therefore higher erosion rates (e.g., Beer & Turowski, 2015; Cook et al., 2013; Foley, 1980; Inoue et al., 2014). The cover effect arises because sediment residing on the bed can shield the bedrock from impacts, thereby decreasing erosion rates (e.g., Chatanantavet & Parker, 2008; Mishra & Inoue, 2020; Turowski, Hovius, Hsieh, et al., 2008). Yet, in landscape evolution models designed for long timescales, fluvial bedrock erosion is commonly described by the stream power incision model (SPIM), in which incision rate is a power function of water discharge and channel bed slope (e.g., Barnhart et al., 2020; Seidl & Dietrich, 1992). The SPIM is unable to account for the tools and cover effects on the process to decadal time scales, but it remains popular because of its simple form. In addition, it explains the widely observed power law scaling between channel bed slope and drainage area, and spatial patterns of knickpoint migration speeds (see Lague, 2014, for a summary of field evidence in the context of the SPIM).

The gap between mechanistic processes understanding on short timescales, and the popularity of the SPIM on long timescales currently represents a central challenge in the study of bedrock channel morphodynamics (Venditti et al., 2020). Diverse temporal scales can be theoretically connected by explicit upscaling, integrating instantaneous process descriptions over the distributions of forcing variables (e.g., Blom et al., 2017; Lague et al., 2005). Attempts to upscale sediment-flux-dependent incision models in this way have so far been scarce, because multiple interacting variables make analytical solutions challenging. Turowski et al. (2007) partitioned sediment-carrying and clean flows using a method suggested by Sklar and Dietrich (2006) in an analytical model of bedrock channel morphology including both tools and cover effects. Lague (2010) included the cover effect, but not the tools effect, into a numerical model of bedrock channel evolution, forced by random time series of daily discharge following an inverse gamma distribution (Crave & Davy, 2001). None of these attempts captures the entire range of conditions and dynamic behavior that can be expected for natural bedrock rivers.

Here, I present analytical solutions for the long-term incision rate and steady state channel morphology using a mechanistic incision law including both tools and cover effects. The solutions demonstrate that the steady state channel long profile is set by bedload transport rather than bedrock incision processes, and offers insights into the role of thresholds and channel width, and the river's adjustment to variable discharge.

2. Theoretical Treatment

In this section, I develop a description of a steady state bedrock channel, upscaling from a sediment-flux-dependent erosion law including both tools and cover effects. Several stochastically varying forcing variables, including water discharge and bedload transport rate, and dependent variables such as bed cover that may exhibit a strong history dependence, are addressed in turn to explain the assumptions made to make an analytical solution possible. By the end, solutions for the long-term mean sediment transport rate, bed cover and incision rate are obtained.

2.1. General Consideration

In previous treatments, water discharge was assumed to be the only stochastically fluctuating parameter. In this case, to upscale instantaneous incision laws to long time scales, we need to integrate over the distribution of discharge, assumed to follow the inverse gamma distribution (e.g., Crave & Davy, 2001; Lague et al., 2005; Molnar et al., 2006)

$$\text{pdf}(Q^*) = \frac{k^{k+1}}{\Gamma(k+1)} \exp\left\{-\frac{k}{Q^*}\right\} Q^{*-(2+k)}. \quad (1)$$

Here, $Q^* = Q / \bar{Q}$ is the instantaneous discharge Q normalized by the long-term mean discharge \bar{Q} , the constant k is a measure of the variability of discharge. For natural streams, k takes typical values between 0.1 and 5 (Molnar et al., 2006). Note that k decreases with increasing discharge variability, that is, $k = 0.5$ signifies a channel with highly variable discharge and $k = 3$ signifies a channel with little discharge variability. $\exp\{x\}$ denotes the natural exponential function, and $\Gamma(x)$ denotes the gamma function, defined by

$$\Gamma(x) = \int_0^{\infty} \exp\{-z\} z^{x-1} dz. \quad (2)$$

Here, z is a dummy variable. The long-term mean of a particular discharge-dependent quantity X of interest can be obtained by integrating over the distribution

$$\bar{X} = \int_{Q_{\min}}^{Q_{\max}} X(Q^*) \text{pdf}(Q^*) dQ^*. \quad (3)$$

Here, Q_{\min} and Q_{\max} denote the minimum and maximum discharge considered to be relevant for setting X , and the overbar denotes the long-term mean of a parameter, as obtained by the integral in Equation 3. For the analysis in the paper, I assume that Q_{\max} is sufficiently high such that the distribution of discharge is adequately captured by integrating the right-hand power law tail of the discharge distribution to infinity (see Lague et al., 2005, for a detailed discussion of the effects of this assumption). Then, Equation 3 becomes

$$\bar{X} = \frac{k^{k+1}}{\Gamma(k+1)} \int_{Q_{\min}}^{\infty} X(Q^*) \exp\left\{-\frac{k}{Q^*}\right\} Q^{*-(2+k)} dQ^*. \quad (4)$$

When dealing with sediment-flux-dependent incision laws, the bedload transport rate is another driving variable affecting incision rates directly via the tools effect and indirectly via the cover effect. Bedload transport rates can fluctuate strongly, and measured rates can scatter over several orders of magnitude for a given discharge (e.g., Turowski, 2010). In addition, the amount of sediment residing on the bed, which determines bed cover, is a history-dependent state variable. Integrating explicitly over the temporal variation of these variables would prevent an analytical treatment and necessitate a numerical solution. To deal with this problem, I introduce an intermediate timescale. At this timescale, the short-term fluctuations of bedload transport rates and sediment cover are averaged out, and the average can be treated as a deterministic function of discharge. To clearly distinguish the quantities at the two timescales, I use the term “average” and angle brackets $\langle \rangle$ for the intermediate timescale, and the term “mean” and an overbar for the geological timescale.

2.2. Treatment of Channel Width

A fully dynamic model of bedrock channel width in a sediment-flux-dependent setting is currently not available. Commonly, channel width is assumed to depend on discharge according to a power law, using standard downstream and at-a-station hydraulic geometry relationships of the form (e.g., Lague et al., 2005)

$$\bar{W} = k_W \bar{Q}^{\omega_d}, \quad (5)$$

and

$$W = \bar{W} Q^{*\omega_a}. \quad (6)$$

Here, \bar{W} is the channel width corresponding to the long-term mean discharge at a particular station, W is the instantaneous width varying locally with discharge, and ω_d and ω_a are dimensionless exponents. Within the present treatment, I replace Equation 5 with the steady state width equation obtained from the model of Turowski (2018)

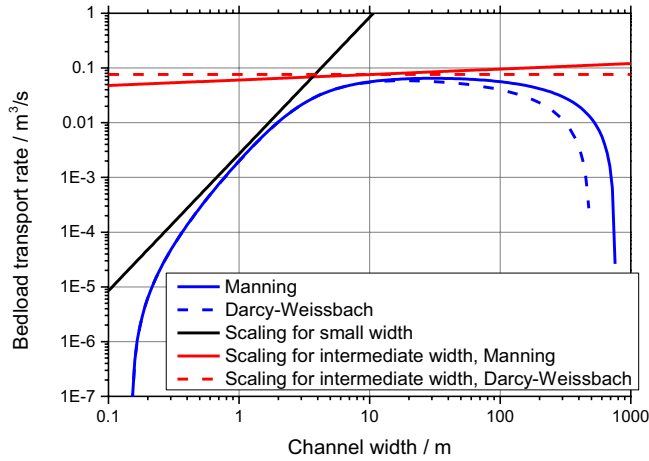


Figure 1. Illustration of the dependence of bedload transport rate on channel width, calculated using a common shear-stress-dependent bedload equation (Fernandez Luque & van Beek, 1976; Meyer-Peter & Müller, 1948) combined with the Manning roughness equation (solid blue line) and the Darcy-Weissbach roughness equation (dashed blue line) (see Appendix A). Note that the threshold of motion cuts off the relationship both for large width, because flow depth becomes too small for transport to occur, and for small width, because shear stress is partitioned from the bed to the channel walls (e.g., Turowski, Hovius, Hsieh, et al., 2008). The scaling bracketing the relationship for small width, giving $q = 5/2$ (black line), for intermediate width using the Darcy-Weissbach friction equation, giving $q = 0$ (dashed red line), and the Manning equation, giving $q = 1/10$ (solid red line), are indicated (see Appendix A). The plot was generated using Equations A1, A8, A9, and A10 (Appendix A), with $\tau_c^* = 0.045$, $k_v = 10$, $\gamma = 4$, and $D = 0.01$ m.

(Carson & Griffiths, 1987; Cook et al., 2020), depending on the sediment transport and flow velocity equations that are used (Figure 1, Appendix A). Note that, depending on the choice of bedload transport equation, m , n , and q are not independent of each other (Appendix A). Using the normalized discharge Q^* , the bedload transport rate can be rewritten as

$$\langle Q_s \rangle = k_{BL} \bar{Q}^m \left(Q^{*m} - Q_{ct}^{*m} \right) W^q S^n. \quad (9)$$

Combining Equation 9 with Equations 6 and 7, we obtain

$$\langle Q_s \rangle = k_{BL} \left(k_e d \frac{\bar{Q}_s}{I} \right)^{q/2} Q^{*q\omega_a} \bar{Q}^m \left(Q^{*m} - Q_{ct}^{*m} \right) S^n. \quad (10)$$

Using Equation 4, the long-term sediment flux is then given by

$$\bar{Q}_s = \frac{k^{k+1}}{\Gamma(k+1)} k_{BL} \left(k_e d \frac{\bar{Q}_s}{I} \right)^{q/2} \bar{Q}^m S^n \int_{Q_{ct}^*}^{\infty} \exp \left\{ -\frac{k}{Q^*} \right\} \left(Q^{*q\omega_a+m-(2+k)} - Q_{ct}^{*m} Q^{*q\omega_a-(2+k)} \right) dQ^*. \quad (11)$$

The integral evaluates to

$$\bar{Q}_s = F_{Q_s} k_{BL} \left(k_e d \frac{\bar{Q}_s}{I} \right)^{q/2} \bar{Q}^m S^n = F_{Q_s} k_{BL} \bar{W}^q \bar{Q}^m S^n. \quad (12)$$

Here, F_{Q_s} is function of the form

$$\bar{W} = \left(k_e d \frac{\bar{Q}_s}{I} \right)^{1/2}. \quad (7)$$

Here, k_e is a measure of the bedrock erodibility, Q_s is the bedload transport rate and I the incision rate, and the sideward deflection distance d is the distance by which bedload particles can be deflected in the cross-channel direction (Turowski, 2018). Here, d is treated as a constant, which can be viewed as a general scaling factor with unit of length within the context of long-term channel morphology.

2.3. Upscaling Bedload Transport

Bedload transport rate can fluctuate strongly even if hydraulic conditions stay constant over time (e.g., Turowski, 2010). However, at a given discharge, there exists a well-defined mean transport rate that scales with discharge. At the intermediate timescale, I assume short-term fluctuations of transport rates can be neglected, and average bedload supply at a given discharge is a function of discharge and slope of the form (e.g., Rickenmann, 2001; Smith & Bretherton, 1972)

$$\langle Q_s \rangle = k_{BL} \left(Q^m - Q_{ct}^m \right) W^q S^n. \quad (8)$$

Here, k_{BL} is a dimensional constant, S is the channel bed slope, Q_{ct} is the critical discharge for the onset of bedload transport m , n , and q are dimensionless exponents, and the angle brackets denote the average quantity at a given discharge at the intermediate time scale. Many standard sediment transport formulas can be expressed in the form of Equation 8. The power function of channel width W is included to make possible the modeling of the varying scaling of sediment flux with channel width

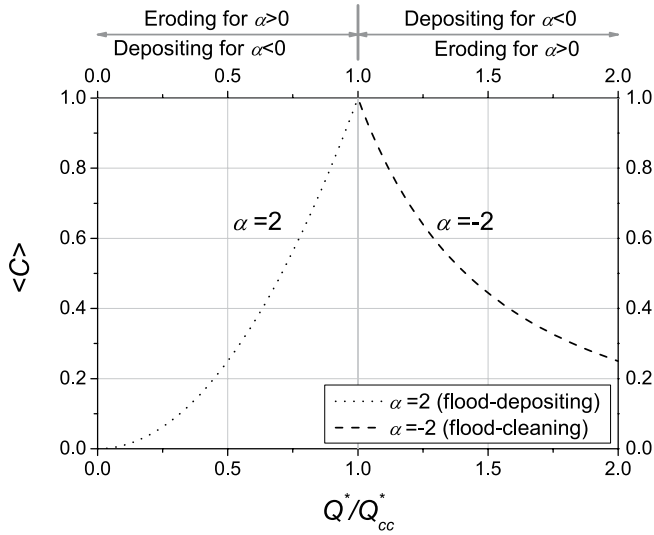


Figure 2. Illustration of the scaling relationship of cover with discharge and the definitions of flood-cleaning and flood-depositing channels (adapted from Turowski et al., 2013). For the flood-depositing case, where cover exponent $\alpha > 0$, the covered fraction of the bed increases with increasing discharge, implying that the bed is partially covered at discharge smaller than the characteristic discharge Q_{cc}^* and fully covered at discharges above it. Bedrock erosion occurs at low and intermediate discharges. For the flood-cleaning case, where the cover exponent $\alpha < 0$, the covered fraction of the bed decreases with increasing discharge, implying that the bed is partially covered at discharge larger than the characteristic discharge Q_{cc}^* and fully covered at discharges below it. Bedrock erosion occurs during floods.

$$F_{Q_s} = \frac{k^{q\omega_a}}{\Gamma(k+1)} \left[k^m \left(\Gamma(k+1-q\omega_a-m) - \Gamma\left(k+1-q\omega_a-m, \frac{k}{Q_{ct}^*}\right) \right) - Q_{ct}^{*m} \left(\Gamma(k+1-q\omega_a) - \Gamma\left(k+1-q\omega_a, \frac{k}{Q_{ct}^*}\right) \right) \right] \quad (13)$$

The upper incomplete gamma function is defined by

$$\Gamma(x, c) = \int_c^\infty \exp\{-z\} z^{x-1} dz. \quad (14)$$

2.4. Upscaling Bed Cover

Bed cover C can vary over short timescales, and is dependent on the history of sediment supply and hydraulic forcing (e.g., Fernández et al., 2019; Lague, 2010; Turowski & Hodge, 2017). However, response timescales of bed cover to varying flow conditions are orders of magnitudes smaller than those of the adjustment of channel width and slope (Turowski, 2020). As a result, similar to bedload transport, cover can be treated to be independent of discharge at the intermediate timescale, following a distribution with a well-defined average for a given discharge. This implies that instantaneous cover C can be viewed as independent of discharge, and the intermediate-term average cover $\langle C \rangle$ systematically varies with discharge. Here, the relationship between the average cover and discharge is modeled by a power law function with a scaling exponent α (Turowski et al., 2013), from hereon called the cover exponent (Figure 2). The bed changes from fully to partially covered at a characteristic dimensionless discharge Q_{cc}^* . When $\alpha > 0$, bed cover increases with increasing discharge, and the bedrock is exposed during small flows, for $Q^* < Q_{cc}^*$. This is the flood-depositing case, for which the cover function is given by

$$\langle C \rangle = \begin{cases} 1 & \text{for } Q^* \geq Q_{cc}^* \\ \left(\frac{Q^*}{Q_{cc}^*} \right)^\alpha & \text{for } 0 \leq Q^* < Q_{cc}^* \end{cases} \quad (15)$$

When $\alpha < 0$, bed cover decreases with increasing discharge, and bedrock is exposed during large flows, for $Q^* > Q_{cc}^*$. This is the flood-cleaning case, for which the cover function is given by

$$\langle C \rangle = \begin{cases} 1 & \text{for } 0 \leq Q^* \leq Q_{cc}^* \\ \left(\frac{Q^*}{Q_{cc}^*} \right)^\alpha & \text{for } Q^* > Q_{cc}^* \end{cases} \quad (16)$$

For convenience, the cover threshold can be written as a multiple b of the threshold discharge Q_{ct}^* for the onset of bedload transport. The ratio b is defined as

$$b = \frac{Q_{cc}^*}{Q_{ct}^*}. \quad (17)$$

With the assumptions made so far, the system features two discharge thresholds, one for the onset of bedload motion and therefore the activity of the tools effect, the other for the change of fully to partially covered

Table 1
The Ranges of Q^* for Which Erosion is Possible in the Four Cases

		Cover threshold larger than threshold of motion	Threshold of motion larger than cover threshold
Cover behavior		$Q_{ct}^* \leq Q_{cc}^* (b \geq 1)$	$Q_{ct}^* > Q_{cc}^* (b < 1)$
Flood-cleaning	$\alpha < 0$	$Q^* \geq Q_{cc}^*$	$Q^* \geq Q_{ct}^*$
Flood-depositing	$\alpha > 0$	$Q_{cc}^* \geq Q^* \geq Q_{ct}^*$	No erosion possible ^a .

^aBedload transport occurs and tools are available only at large discharges, when the bed is fully covered.

bed. Together with the two types of cover behavior of the channel (Figure 2), flood-depositing ($\alpha > 0$, Equation 15) and flood-cleaning ($\alpha < 0$, Equation 16), we can distinguish four cases, yielding different integrative limits and solutions for the long-term results (Table 1). In the flood-cleaning case, when $Q_{ct}^* \leq Q_{cc}^* (b > 1)$, erosion occurs for all discharges greater than Q_{cc}^* . In the flood-cleaning case, when $Q_{ct}^* > Q_{cc}^* (b < 1)$, erosion occurs for all discharges greater than Q_{ct}^* . In the flood-depositing case, when $Q_{ct}^* \leq Q_{cc}^* (b > 1)$, erosion occurs for all discharges greater than Q_{ct}^* and smaller than Q_{cc}^* . In the flood-depositing case, when $Q_{ct}^* > Q_{cc}^* (b < 1)$, no erosion occurs, because bedload moves and tools are only available at discharges when the bed is fully covered. For the three cases in which erosion occurs at some discharges, Equation 4 can be applied to calculate the long-term mean cover. The solutions have the general form

$$\bar{C} = F_C(k, Q_{ct}^*, Q_{cc}^*, m, \alpha). \quad (18)$$

Here, F_C is a dimensionless function. Full solutions for F_C are given in Appendix B.

2.5. Upscaling Sediment-Flux-Dependent Incision

A sediment-flux-dependent erosion law, including tools and cover effects, can be given by (Auel et al., 2017; Sklar & Dietrich, 2004; Turowski, 2018; Zhang et al., 2015):

$$I = k_e \frac{Q_s}{W} (1 - C). \quad (19)$$

The dimensional constant k_e depends on rock, sediment, and fluid properties, given by Auel et al. (2017) as

$$k_e = \frac{gY}{230k_v\sigma_T^2} \left(\frac{\rho_s}{\rho} - 1 \right). \quad (20)$$

Here, g is the acceleration due to gravity, Y is Young's modulus of the bedrock, σ_T its tensile strength, k_v is the dimensionless rock resistance coefficient, and ρ_s and ρ are the sediment and fluid density, respectively. At the intermediate timescale, Equation 19 can be rewritten as

$$I = k_e \frac{\langle Q_s \rangle}{W} (1 - \langle C \rangle). \quad (21)$$

Combining Equations 4, 6, 7, 10, 12, 13, 17, 18, and 21, the long-term incision rate can be evaluated by the integral

$$\bar{I} = \frac{k^{k+1}}{\Gamma(k+1)} k_e k_{BL} \left(k_e d \frac{\bar{Q}_s}{I} \right)^{q-1/2} \bar{Q}^m S^n \int_{Q_{min}^*}^{Q_{max}^*} Q^{*(q-1)\omega_a} (Q^{*m} - Q_{ct}^{*m}) \left(1 - \left(\frac{Q^*}{Q_{cc}^*} \right)^\alpha \right) \exp \left\{ -\frac{k}{Q^*} \right\} Q^{*-(2+k)} dQ^*. \quad (22)$$

Here, the limits of integration Q_{min}^* and Q_{max}^* depend on the values of α and b (see Table 1). The full solutions for all three cases are given in Appendix C, and take the general form

$$\bar{I} = k_e k_{BL} \left(k_e d \frac{\bar{Q}_s}{I} \right)^{q-1/2} \bar{Q}^m S^n F_I(k, Q_{ct}^*, Q_{cc}^*, m, q, \omega_a, \alpha) = k_e \frac{\bar{Q}_s}{W} \frac{F_I}{F_{Q_s}}. \quad (23)$$

Here, $F_I(k, Q_{ct}^*, Q_{cc}^*, m, q, \omega_a, \alpha)$ is a dimensionless function depending on the values of α and b (Appendix C).

Table 2

Parameter Values Used for the Example Calculations, Following Estimates for the Liwu River, at Lushui, Taiwan (Turowski, 2020; Turowski et al., 2007)

Parameter	Symbol	Value
Material properties		
Density of water (kg/m ³)	P	1,000
Density of sediment (kg/m ³)	ρ_s	2,650
Young's modulus (MPa)	Y	5×10^4
Rock tensile strength (MPa)	σ_T	10
Rock resistance coefficient	k_v	10^6
Constants in the equations		
Acceleration due to gravity (m/s ²)	g	9.81
Flow velocity friction coefficient	k_V	10
Bedload discharge exponent	m	1
Bedload slope exponent	n	2
Bedload coefficient (kg/m ³)	K_{bl}	11,000
Critical shields stress	θ_c	0.045
Channel reach parameters		
Drainage area (km ²)	A	435
Elevation (m)		410
Channel bed slope	S	0.02
Channel width (m)	W	36.7
At-a-station width exponent	ω_a	0.4
Scaling length (deflection length scale) (m)	d	0.1
Median grain size (m)	D	0.04
Daily average water discharge (m ³ /s)	Q	36
Dimensionless threshold discharge of motion	Q_{ct}^*	0.15
Discharge variability parameter	k	3
Sediment supply (kg/s)	Q_s	200
Long-term bedload fraction	$\bar{\beta}$	0.3
Long-term incision rate (mm/yr)	\bar{I}	1

3. Results

In general, there are four unknown variables, channel bed slope S , the long-term cover fraction \bar{C} (Equation 18; see also Appendix B, Equations B3, B6, and B9), the long-term bedload sediment supply \bar{Q}_s (Equation 12), and the ratio between the cover threshold and the threshold of bedload motion b (Equation 16). The solutions provide three equations. The long-term incision rate \bar{I} (Equation 23) can be treated as an independent variable that is determined by the long-term uplift or baselevel lowering rate. Another equation can be obtained from the conditions for steady state, when the long-term bedload supply is related to the long-term incision rate by

$$\bar{Q}_s = \bar{\beta} A \bar{I}. \quad (24)$$

Here, $\bar{\beta}$ is the long-term mean fraction of sediment that is transported as bedload, and A is the drainage area. I further substitute discharge with a simple hydrologic relation

$$\bar{Q} = \bar{R} A. \quad (25)$$

Here, \bar{R} is the long-term mean runoff. To illustrate the dependence of channel morphology and of the adjustment time scales on control and channel morphology parameters, I used parameter values oriented on Lushui at the Liwu River, Taiwan (Table 2; see Turowski et al., 2007, and Turowski, 2020). The values of reach parameters were either measured in the field or estimated using literature data.

3.1. Steady State Channel Long Profile

Both long-term bedload supply (Equation 12) and long-term incision rate (Equation 23) show the same dependence on channel bed slope, while long-term mean cover is independent of slope (Appendix B). As a result, channel bed slope S can be calculated from the equation for long-term bedload supply (Equation 12), which is independent of the cover threshold and of long-term cover. Inverting Equation 12 for S and substituting Equations 24 and 25 yields

$$S = F_{Q_s}^{-(1/n)} \left(\frac{\bar{I}}{k_{BL}} \right)^{(1/n)} (k_e d)^{-(q/2n)} \bar{\beta}^{2-q/2n} \bar{R}^{-m/n} A^{(2-2m-q/2n)}. \quad (26)$$

For certain combinations of the parameter values, the function F_{Q_s} may be negative or not give a solution at all. In these cases, Equation 26 does not yield a valid solution for the channel bed slope. Parameter combinations without solutions occur mainly for $1 < k < 2.5$ (Figure 3).

3.2. Scaling With Discharge Variability

The controls on channel morphology by discharge variability k are complicated (Figure 4), and depend both on the cover scaling exponent α and the width scaling exponent q . For the same discharge variability k , multiple possible solutions are available for most of the parameter space. The solution for the channel bed slope S is independent of α , but strongly dependent on q (Figure 4a). For small values of k , S increases with increasing k , for intermediate values of k , no solutions are available (see also Figure 3), and for large values of k , S decreases with increasing k (Figure 4a). The ratio of cover threshold to threshold of motion b (Equation 17), and the long-term mean cover \bar{C} can increase or decrease with

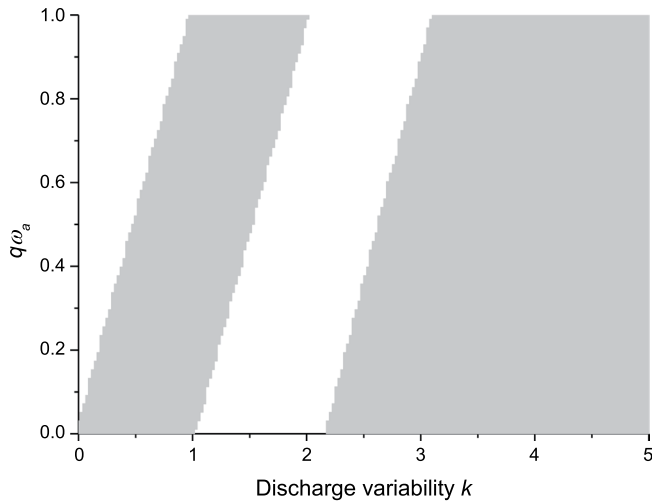


Figure 3. Space of valid solutions of slope (Equation 26) are shown in gray, for a thresholds of motion $Q_{ct}^* = 1$. Other choices for Q_{ct}^* only slightly alter the results.

increasing discharge variability k , depending on the values of q and α (Figures 4b and 4c). The threshold ratio b is weakly dependent on k for $k < 2$ and $k > 3.5$ (Figure 4b). For $2 < k < 3.5$, it decreases strongly with increasing k when $\alpha = 2$, and increases weakly when $\alpha = -2$. The long-term mean cover is constant for $k < 1.5$, regardless of the values of q and α (Figure 4c). For $k > 2.5$, it increases when $\alpha = -2$, but it decreases when $\alpha = 2$.

3.3. Control of Reach-Scale Cover Behavior

The ratio of cover threshold to threshold of motion b (Equation 17), and the long-term mean cover, depends on reach-scale cover behavior, that is, whether the channel behaves as flood-cleaning (when the cover scaling exponent $\alpha < 0$) or flood-depositing ($\alpha > 0$). For flood-cleaning channels, b is close to zero or to one, for flood-depositing channels, it is larger than one (Figure 5a & 5c). For streams with low discharge variability (high k) the long-term mean cover increases for increasing α for flood-cleaning channels, and decreases for increasing α for flood-depositing channels (Figure 5b). For streams with high discharge variability, the function is complicated (Figure 5d)

4. Discussion

4.1. Steady State Channel Long Profile

Empirically, the channel long profile of bedrock rivers is often described by a power law function, as has been observed in many natural settings (e.g., Whipple, 2004; Whitbread et al., 2015):

$$S = k_s A^{-\theta}. \quad (27)$$

Here, k_s is known as the steepness index and θ is known as the concavity index. While the concavity index θ typically falls into a narrow range between 0.4 and 0.7 in natural bedrock channels (e.g., Lague, 2014; Whipple, 2004), the value of the steepness index k_s can vary over several orders of magnitude (e.g., Barnhart et al., 2020). The upscaled model yields a similar slope-area scaling (Equation 26; Figure 6), in which the steady state channel long-profile is controlled by the mechanics of bedload transport, rather than the mechanics of bedrock incision. This notion is consistent with field observations of Johnson et al. (2009). Assuming that the long-term average bedload fraction $\bar{\beta}$ scales with drainage area A according to

$$\bar{\beta} = k_\beta A^{-B}. \quad (28)$$

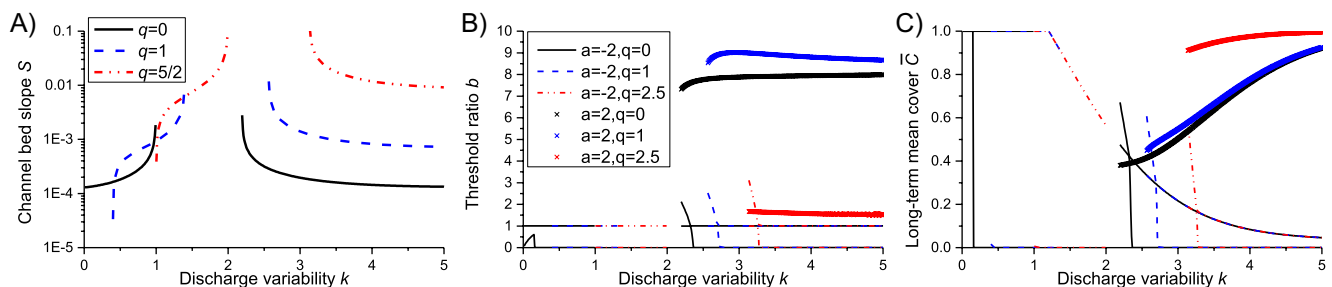


Figure 4. (a) Scaling of slope S (Equation 26) (b) the ratio of cover threshold to threshold of motion b (Equation 17), and (c) of the long-term mean cover \bar{C} with the discharge variability parameter k . Lines for the cover exponent $\alpha = -2$ (flood-cleaning), crosses for $\alpha = 2$ (flood-depositing). Black for the width exponent $q = 0$, blue for $q = 1$, and red for $q = 2.5$. Note that channel bed slope is independent of α (Equation 26). For many conditions, there are two solutions available, corresponding to the solutions for b smaller (dashed) or larger than one (solid) (see Table 1; Appendices B and C).

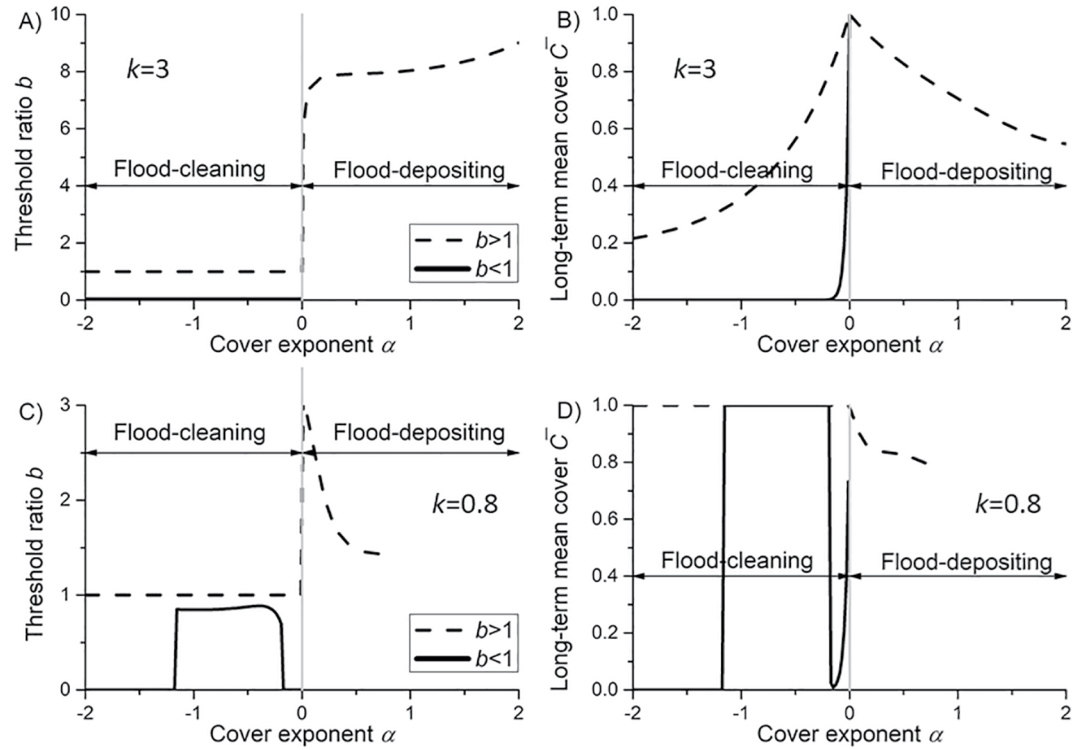


Figure 5. (a and c) Scaling of the ratio of cover threshold to threshold of motion b (Equation 17) and (b and d) of the long-term mean cover with the cover scaling exponent α (see Equations 15 and 16), for a (a and b) low variability ($k = 3$); and (c and d) high variability climate ($k = 0.8$). For flood-cleaning streams ($\alpha < 0$) (cf. Figure 2, Table 1), separate solutions are shown for the threshold ratio b (Equation 17), for $b > 1$ (dashed line) and $b < 1$ (solid line).

The concavity index θ is then given by

$$\theta = \frac{2m - (1 - B)(2 - q)}{2n}. \quad (29)$$

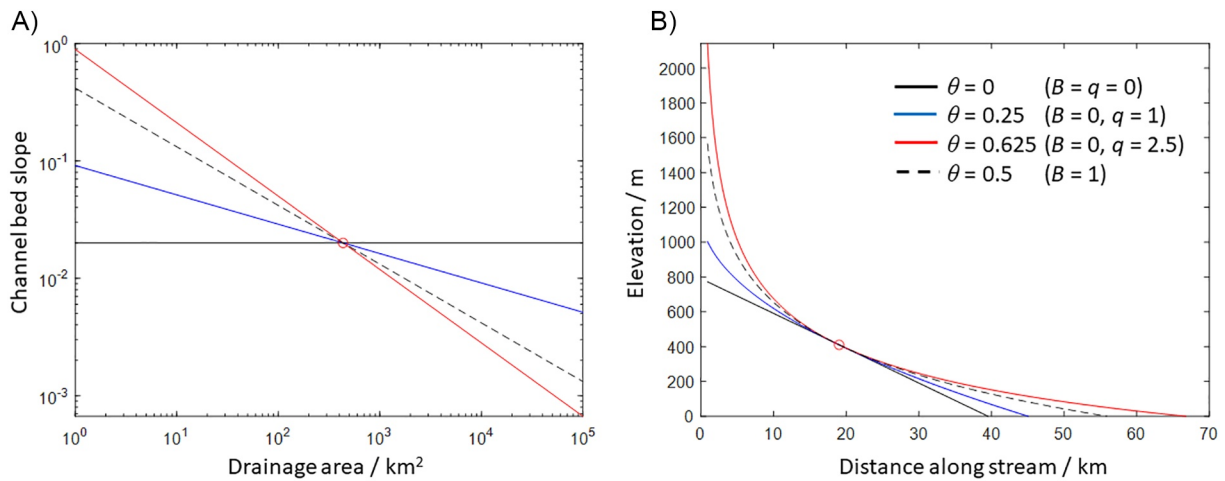


Figure 6. (a) Slope-area relationship predicted by the model (Equation 26) and (b) corresponding elevation profiles. The concavity index θ was calculated using Equation 29. Relationships are shown for $m = 2$ and $n = 1$, and $B = q = 0$ (black line), $B = 0$ and $q = 1$ (blue line), $B = 0$ and $q = 2.5$ (red line), and $B = 1$ (black dashed). The steepness index was calibrated to the conditions at the Liwu (red circle, Table 2), with $A = 435 \text{ km}^2$, $S = 0.02$ (Table 2), and elevation 410 m. Hack's law $A = k_H \ell^H$ was used to convert from drainage area to channel length, with $k_H = 1.2$ and $H = 2$.

The bedload fraction typically decreases with increasing drainage when different river catchments are compared (Turowski et al., 2010). Based on field observations in the Himalayas, Dingle et al. (2017) suggested that the bedload transport rate in actively eroding rivers is constant along a river, despite increasing drainage area, implying $B = 1$ for a steady state catchment (cf. Equation 24). In the following, I will discuss the endmember cases of $B = 1$ (bedload transport rate independent of drainage area) and $B = 0$ (bedload fraction independent of drainage area). In the former case, for $B = 1$, the concavity index is equal to the ratio of the discharge and slope exponents in the bedload transport Equation 8, m/n , independent of the value of q . In the latter case, for $B = 0$, a wide range of values can be obtained for concavity index, depending on the choices for m , n , and q . In natural rivers, θ is usual within the range between 0.4 and 0.7 (Lague, 2014; Whipple, 2004). A value of $\theta = 5/8 = 0.625$ is obtained for $m = 1$ and $n = 2$, as in the bedload transport equation of Rickenmann (2001) (see also the discussion of Turowski, 2018), and $q = 5/2$, corresponding to the limit behavior for narrow channels (Figure 1; Appendix A). Smaller values of q decrease the concavity, with $\theta = 0$ for $q = 0$, and $\theta = 1/4 = 0.25$ for $q = 1$. A value of $\theta = 0.5$, a standard choice in many modeling exercises, is obtained for $q = 2$.

The channel long-profile solution of the upscaled model (Equation 26) gives an explicit expression for the steepness index in terms of long-term incision rate \bar{I} , erodibility k_e (Equation 20), long-term mean bedload fraction $\bar{\beta}$, long-term mean runoff \bar{R} , as well as channel geometry parameters (e.g., the width exponent q) and discharge variability k :

$$k_s = F_{Qs}^{-1/n} \left(\frac{\bar{I}}{k_{BL}} \right)^{(1/n)} (k_e d)^{-(q/2n)} k_\beta^{(2-q/2n)} \bar{R}^{-(m/n)}. \quad (30)$$

Here, F_{Qs} is given by Equation 13. The steepness index k_s can in principle be calibrated to measurable parameters (Appendix D). The formulation helps explaining the large variability observed for the steepness index in nature. For example, erodibility depends on the inverse square of rock tensile strength (Equation 20), which varies over more than 2 orders of magnitude for natural rock (e.g., Sklar & Dietrich, 2001). In addition, Equation 30 allows stream profile inversions for incision rate (e.g., Wobus et al., 2006) with considerably more detail than the commonly used SPIM. However, many of the necessary parameters, such as the width exponent q , are not usually known for natural channels, and would require extensive field measurements. As a result, no data sets are currently available that include all necessary parameter values for natural channels. Therefore, a full test of the model is currently not possible.

The lack of valid solutions for channel bed slope for certain parameter combinations (Figure 4) occurs when the sum of four terms including the gamma or incomplete gamma functions in Equation 13 are equal to or smaller than zero. The values of the four terms depend on discharge variability k , the discharge exponent m in the bedload transport equation (Equation 8), and the product of the width exponent q (Equation 8) and the at-a-station hydraulic geometry exponent for width, ω_a (Equation 6). This suggests that the river needs to adjust its absolute width (which changes the width exponent q) and its at-a-station hydraulic geometry for width (i.e., the cross-sectional shape, which changes ω_a) to achieve a channel long-profile that is consistent with the condition of grade, in which sediment deposition and entrainment are balanced. The results underline the importance of channel width for understanding bedrock channel dynamics.

4.2. Cover and Thresholds

According to the model, long-term channel dynamics are controlled by at least two discharge thresholds, the critical discharge for the onset of bedload motion, and the discharge at which the channel switches from a fully to a partially covered bed. The relationship between these two threshold discharges, quantified in their ratio b , depends strongly both on the reach-scale cover behavior (quantified by the cover scaling exponent α ; see Figure 5a) and discharge variability k (Figure 5b). Often multiple solutions for the channel geometry are available for the same set of boundary conditions (Figure 4). Turowski et al. (2013) showed that both flood-cleaning ($\alpha < 0$) and flood-depositing ($\alpha > 0$) bedrock channels exist in nature, and sometimes reaches behaving one way or the other alternate in a single stream (e.g., Heritage et al., 2004). It is unclear what controls the cover scaling exponent α , and correspondingly, why a particular reach or stream behaves

flood-cleaning or flood-depositing. It can be expected that both hillslope processes and in-channel processes contribute to this control (cf. Turowski et al., 2013). For example, precipitation amount and intensity control hillslope sediment supply to the channel by landsliding or surface wash, but also the in-channel sediment transport capacity via their relationship to discharge. Water discharge, in turn, affects upstream sediment supply to a given reach, as well as bank and bed erosion rates. The cover exponent α could be related to or depend on other parameters such as discharge variability k , and the cross-sectional shape, quantified by the at-a-station hydraulic geometry exponent for width, ω_a , and the width exponent q . All four of these parameters are treated as independent variables in the model, but may adjust their values through yet unknown feedback mechanisms. These topics provide starting points for future research. The parameters ω_a , k , and α can be obtained from field observations. The hydraulic geometry exponent ω_a can be constrained from parallel measurements of width and discharge (e.g., Turowski, Hovius, Wilson, & Horng, 2008), and the cover exponent α from parallel observations of cover and discharge. To estimate the discharge variability parameter k , a discharge time series is necessary spanning at least a few years, better decades (e.g., Molnar et al., 2006). The deflection length scale d is likely difficult to measure in natural settings, but should be well suited for study in laboratory experiments.

The combination of a flood-depositing channel with a threshold discharge for the onset of bedload motion that is higher than the discharge at which the bed becomes fully alluviated allows for a solution in which no incision occurs. Bedrock channels may evolve to this state when tectonic activity of a mountain belt ceases and uplift stops, rather than turning into an alluvial channel.

4.3. Upscaling Instantaneous and Intermediate Timescale Process Descriptions

In the description of long-term evolution of river channels or entire landscapes, it is common to upscale instantaneous or intermediate timescale process descriptions by substituting a representative long-term discharge for the instantaneous or intermediate discharge. The upscaled version for bedload transport (Equation 12) resembles the process description at intermediate timescales (Equation 8), similar to the upscaled version of the SPIM (Lague et al., 2005). There are three key differences: (i) instantaneous and intermediate timescale variables are replaced by their long-term equivalents, (ii) the threshold vanishes in the long-term equation, and (iii) a dimensionless function, dependent on discharge variability k , channel morphology parameters, ω_a , and q , and thresholds, such as the threshold of sediment motion Q_{ct} , is multiplied on (e.g., Equation 13). In contrast, the upscaled equations for bed cover (Equation 18) does not resemble the intermediate timescale version (Equations 15 and 16). In comparison to the instantaneous incision rate (Equation 19), in the equation for the upscaled incision rate (Equation 23) the dependence on cover is replaced by a different dimensionless function (Appendix C). As such, while equations similar to the instantaneous process law can be used in the long term, the determination of the dimensionless scaling factor may be complicated, and depend, for example, on the discharge variability parameter k . Both channel bed slope S (Figure 4a) and the threshold ratio b (Figure 4b) become independent of the discharge variability parameter k for large k , corresponding to small discharge variability. Consistent with previous notions (cf. Deal et al., 2018; Lague et al., 2005), this may imply that discharge variability does not need to be precisely known for environments with high k (low variability), when channel slope S is the primary interest. However, the long-term cover \bar{C} behaves in the opposite way (Figure 4c), with constant values for small k and high variability for large k . Further, the relationship between the threshold ratio b and the cover exponent α are strongly modulated by k (Figures 5a and 5c), and slope depends on q even for large k . Again, questions about the feedbacks between α , the discharge variability parameter k , the cross-sectional shape, quantified by the at-a-station hydraulic geometry exponent for width, ω_a , and the width exponent q arise and provide starting points for future research.

4.4. Comparison to the Upscaled Stream-Power Incision Model

The upscaled SPIM (Appendix E; Lague et al., 2005) is able to capture the nonlinear dependence of incision rates on discharge variability observed in the Himalaya (DiBiase & Whipple, 2011; Scherler et al., 2017). The results obtained from sediment-flux-dependent incision models give similar relationships for flood-cleaning channels and a ratio of cover threshold to threshold of motion b that is smaller than one (Figure 7). How-

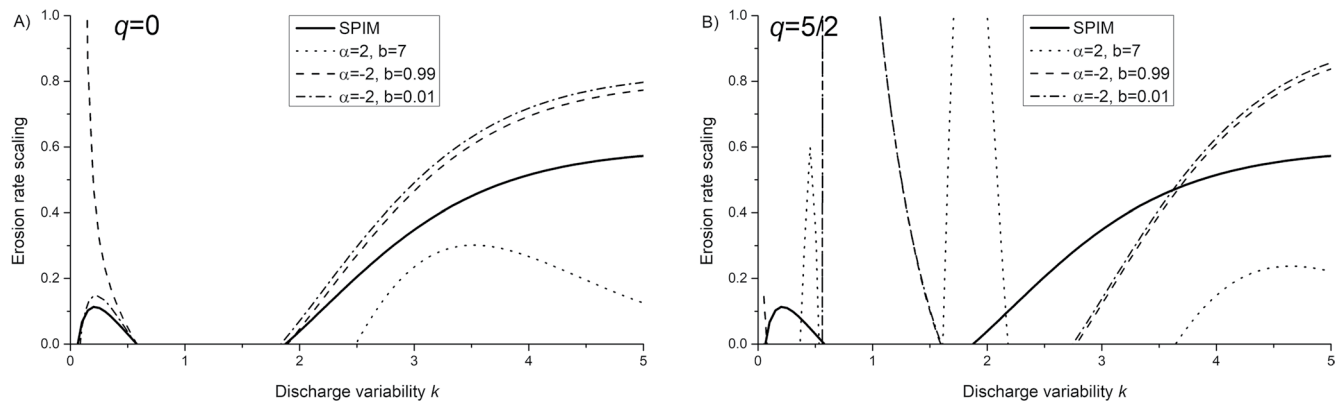


Figure 7. Comparison of the dependence of incision rate on discharge variability k obtained from the stream power incision model (SPIM, solid line; see Appendix E) and the sediment-flux-dependent model used herein (see Appendix C). Calculations were made for values of the width exponent of (a) $q = 0$ and (b) $q = 5/2$ (see Appendix A), and a threshold of motion $Q_{cr}^* = 1$.

ever, they yield several other potential solutions, indicating a larger flexibility of the channel to deal with different climatic situations.

The model presented here uses a sediment-flux-dependent bedrock incision models rooted in current mechanistic understanding of fluvial bedrock incision. As such, it connects reach-scale to landscape-scale approaches in modeling bedrock river dynamics, addressing what Venditti et al. (2020) called a current grand challenge of geomorphology. The channel long profile predicted by the model yields a power-law dependence of channel bed slope on incision rate and drainage area similar to the one obtained from the stream-power incision model (SPIM) (Equation 26). The SPIM has been claimed to provide a description of bedrock channel dynamics on long time scales (e.g., Venditti et al., 2020), even though its mechanistic assumption—a direct scaling between erosion rate and stream power (Seidl & Dietrich, 1992)—has been falsified on the process time scale (e.g., Beer & Turowski, 2015; Sklar & Dietrich, 2001). Whipple and Tucker (2002) already recognized that a wide range of incision models yield similar or even identical predictions for the channel long profile, and concluded that observations of transient dynamics need to be used to assess model efficacy. However, studies that have attempted this arrived at conflicting results. For example, van der Beek and Bishop (2003) found that all of the tested models could be parameterized to explain their observations, while Tomkin et al. (2003) concluded that none of the tested models could be fit to their data with physically meaningful parameter values. Valla et al. (2010) found that a transport-limited model better described their data, while Attal et al. (2011) argued that a SPIM yielded the best fit, provided a threshold of erosion was included. Even though it is limited to steady state channels, the model developed herein yields multiple possible solution for a given set of boundary conditions. It has previously been shown that sediment-flux-dependent incision models can yield transient behavior that mimics either transport- or detachment-limited conditions or a mixture of both (e.g., Davy & Lague, 2009; Gasparini et al., 2007; Whipple & Tucker, 2002). This suggests that sediment-flux-dependent incision models as used here can yield the rich transient behavior inferred from observations in natural bedrock channels (cf. Lague, 2014).

5. Conclusions

Bedrock channels are thought to evolve toward a steady state in which the long-term incision rate is equal to the long-term baselevel-lowering rate (e.g., Lague et al., 2005; Whipple, 2004), but also have the need to transport the supplied sediment load (e.g., Turowski, 2020). Upscaling a sediment-flux-dependent incision model rooted in current mechanistic understanding of fluvial bedrock incision processes yields several solutions that are consistent with the requirements for the long-term steady state, but differ in their short time dynamics, for example in the relationship of bed cover and discharge, or transport capacity and channel width. Some of these solutions are similar to the behavior expected in the stream power paradigm, but other solutions are also possible. In the stream-power incision model, both in its instantaneous and in its upscaled form, the effects of channel width, of sediment supply and transport, and of bedrock erodibility

are lumped together in a single calibration parameter, usually called the erodibility. In contrast, the model presented here makes the relationship of the long-term incision rate and of channel geometry with these effects explicit. It thus advances a more detailed picture into the long-term behavior of bedrock channels and offers a wider range of testable predictions and assumptions.

For certain parameter combinations, the model does not yield a solution for channel bed slope. However, it is in most cases possible to find a solution by adjusting the dependence of the bedload transport capacity on channel width (via the exponent q), the cross-sectional geometry (via the at-a-station hydraulic geometry exponent for width, ω_a), or the reach-scale cover dynamics (via the exponent α). It is unclear what controls these parameters in nature and whether they interdepend on each other. Still, the model results suggest that the long-term dynamic behavior of bedrock channels is richer than previously thought, and that there are controls and feedbacks that have been little explored so far.

The long-term incision rate (Equation 26) is explicitly dependent on bedrock erodibility, channel width, and discharge variability, as well as the free parameters determining reach-scale cover behavior and cross-sectional shape. All of these effects have previously been argued to be important factors in setting incision rates (e.g., Bursztyn et al., 2015; Cook et al., 2013; Lague et al., 2005; Whitbread et al., 2015). However, within the SPIM, they are lumped into a single calibration parameter. The new formulation makes it possible to separate all of these effects. This offers rich new possibilities for testing the model using data from natural streams.

Appendix A: Width Dependence of Bedload Transport Rate

A commonly used equation for bedload transport has the form (e.g., Fernandez Luque & van Beek, 1976; Meyer-Peter & Müller, 1948)

$$Q_s = \gamma W \left(g \left(\frac{\rho_s}{\rho} - 1 \right) D^3 \right)^{1/2} (\tau^* - \tau_c^*)^{3/2}. \quad (\text{A1})$$

Here, γ is a dimensionless coefficient and D is a representative grain size. The reach-averaged Shields stress τ^* is defined by

$$\tau^* = \frac{\tau}{(\rho_s - \rho)gD}. \quad (\text{A2})$$

Here, τ is the shear stress, given by the DuBoys equation

$$\tau = \rho g R_h S. \quad (\text{A3})$$

Here, R_h is the hydraulic radius. The continuity equation for water flow is

$$Q = A_c V. \quad (\text{A4})$$

Here, A_c is the cross-sectional area. For a rectangular channel, hydraulic radius and cross-sectional area are given by

$$A_c = WH, \quad (\text{A5})$$

and

$$R_h = \frac{WH}{W + 2H}. \quad (\text{A6})$$

Here, H is the flow depth. A generic form for the cross-section averaged flow velocity can be written as

$$V = k_V R_h^\delta S^{1/2}. \quad (\text{A7})$$

Here, k_V is a friction coefficient and δ takes the value of $1/2$ for the Darcy-Weissbach equation and $2/3$ for the Manning equation. Eliminating H , R_h , A_c , and V by combining Equations A3–A7, we obtain

$$2Q\left(\frac{\tau}{\rho g}\right) = QSW - k_V W^2 S^{(1/2)-\delta} \left(\frac{\tau}{\rho g}\right)^{1+\delta}. \quad (\text{A8})$$

Equation A8 does not permit a closed-form solution for τ (see Figure 1 for a numerical solution). However, we can make some statements on scaling. If width is small, the quadratic term in width can be neglected. Then

$$\tau \approx \frac{1}{2} \rho g SW. \quad (\text{A9})$$

For intermediate width, the term independent of width on the left-hand side can be neglected, and scales as

$$\tau \approx \rho g \left(\frac{QS}{k_V}\right)^{\frac{1}{1+\delta}} S^{\frac{2\delta-1}{2(1+\delta)}} W^{-\frac{1}{1+\delta}}. \quad (\text{A10})$$

Applying Equations A10 or A11 to the bedload transport Equation A1, we can obtain sensible values for the width exponent q in Equation 8:

$$\langle Q_s \rangle = k_{BL} (Q^m - Q_{ct}^m) W^q S^n. \quad (\text{A11})$$

Using Equation A10, shear stress τ is independent of discharge ($m = 0$), and proportional to both slope and width, and $n = 3/2$ and $q = 5/2$. Using Equation A11, we need to distinguish for the two friction equations. For the Darcy-Weissbach equation, when $\delta = 1/2$, this results in $m = n = 1$ and $q = 0$, while for the Manning equation, when $\delta = 2/3$, this results in $m = 9/10$, $n = 21/20$ and $q = 1/10$. Note that Rickenmann (2001) showed that $n = 2$ gives a better description of field data than the theoretical values given above. He suggested that this deviation results from the decreasing occurrence and importance of macro-roughness elements such as stationary boulders or step-pool sequences when moving downstream.

Appendix B: Solutions for Long-Term Average Cover

For the flood-cleaning case ($\alpha < 0$) with $Q_{ct}^* < Q_{cc}^*$ ($b > 1$) we obtain

$$\langle C \rangle = \begin{cases} 1 & \text{for } 0 < Q^* < Q_{cc}^* \\ \left(\frac{Q^*}{Q_{cc}^*}\right)^\alpha & \text{for } Q_{cc}^* \leq Q^* \end{cases}. \quad (\text{B1})$$

Combining with Equation 4, the integral becomes

$$\bar{C} = \frac{k^{k+1}}{\Gamma(k+1)} \left[\int_0^{Q_{cc}^*} \exp\left\{-\frac{k}{Q^*}\right\} Q^{*-(2+k)} dQ^* + \int_{Q_{cc}^*}^{\infty} \exp\left\{-\frac{k}{Q^*}\right\} \left(\frac{Q^*}{Q_{cc}^*}\right)^\alpha Q^{*-(2+k)} dQ^* \right]. \quad (\text{B2})$$

The integral evaluates to

$$\bar{C} = \frac{1}{\Gamma(k+1)} \left[\Gamma\left(k+1, \frac{k}{bQ_{ct}^*}\right) + k^\alpha b^{-\alpha} Q_{ct}^{*\alpha} \left(\Gamma(k+1-\alpha) - \Gamma\left(k+1-\alpha, \frac{k}{bQ_{ct}^*}\right) \right) \right]. \quad (\text{B3})$$

For the flood-cleaning case ($\alpha < 0$) with $Q_{ct}^* > Q_{cc}^*$ ($b < 1$), we obtain

$$\langle C \rangle = \begin{cases} \left(\frac{Q^*}{Q_{cc}^*} \right)^\alpha & \text{for } Q_{ct}^* \leq Q^* \\ \left(\frac{Q_{ct}^*}{Q_{cc}^*} \right)^\alpha & \text{for } 0 < \frac{Q^*}{Q_{ct}^*} < 1 \end{cases}. \quad (B4)$$

The integral becomes

$$\bar{C} = \frac{k^{k+1}}{\Gamma(k+1)} \left(\int_0^{Q_{ct}^*} \left(\frac{Q_{ct}^*}{Q_{cc}^*} \right)^\alpha \exp\left\{-\frac{k}{Q^*}\right\} Q^{*-(2+k)} dQ^* + \int_{Q_{ct}^*}^{\infty} \left(\frac{Q^*}{Q_{cc}^*} \right)^\alpha \exp\left\{-\frac{k}{Q^*}\right\} Q^{*-(2+k)} dQ^* \right). \quad (B5)$$

Evaluating

$$\bar{C} = \frac{1}{\Gamma(k+1)} \left[b^{-\alpha} \Gamma\left(k+1, \frac{k}{Q_{ct}^*}\right) + k^\alpha b^{-\alpha} Q_{ct}^{*-\alpha} \left(\Gamma(k+1-\alpha) - \Gamma\left(k+1-\alpha, \frac{k}{Q_{ct}^*}\right) \right) \right]. \quad (B6)$$

For the flood-depositing case ($\alpha > 0$) with $Q_{ct}^* < Q_{cc}^*$ ($b > 1$), we obtain

$$\langle C \rangle = \begin{cases} \left(\frac{Q_{ct}^*}{Q_{cc}^*} \right)^\alpha & \text{for } 0 < Q^* < Q_{ct}^* \\ \left(\frac{Q^*}{Q_{cc}^*} \right)^\alpha & \text{for } Q_{ct}^* < Q^* < Q_{cc}^* \\ 1 & \text{for } Q_{cc}^* \leq Q^* \end{cases}. \quad (B7)$$

The integral becomes

$$\bar{C} = \frac{k^{k+1}}{\Gamma(k+1)} \left(\int_0^{Q_{ct}^*} \left(\frac{Q_{ct}^*}{Q_{cc}^*} \right)^\alpha \exp\left\{-\frac{k}{Q^*}\right\} Q^{*-(2+k)} dQ^* + \int_{Q_{ct}^*}^{Q_{cc}^*} \left(\frac{Q^*}{Q_{cc}^*} \right)^\alpha \exp\left\{-\frac{k}{Q^*}\right\} Q^{*-(2+k)} dQ^* + \int_{Q_{cc}^*}^{\infty} \exp\left\{-\frac{k}{Q^*}\right\} Q^{*-(2+k)} dQ^* \right). \quad (B8)$$

Evaluating

$$\bar{C} = \frac{1}{\Gamma(k+1)} \left[b^{-\alpha} \left(\Gamma\left(k+1, \frac{k}{Q_{ct}^*}\right) + k^\alpha b^{-\alpha} Q_{ct}^{*-\alpha} \left(\Gamma\left(k+1-\alpha, \frac{k}{bQ_{ct}^*}\right) - \Gamma\left(k+1-\alpha, \frac{k}{Q_{ct}^*}\right) \right) \right) + \left(\Gamma(k+1) - \Gamma\left(k+1, \frac{k}{bQ_{ct}^*}\right) \right) \right]. \quad (B9)$$

Appendix C: Solutions for the Long-Term Incision Rate

For the flood-cleaning case ($\alpha < 0$) with $Q_{ct}^* < Q_{cc}^*$ ($b > 1$), we obtain

$$\begin{aligned} \bar{I} = & k_e k_{BL} \left(k_e d \frac{\bar{Q}_s}{\bar{I}} \right)^{q-1/2} \bar{Q}^m S^n \frac{k^{(q-1)\omega_a}}{\Gamma(k+1)} \left[k^m \Gamma \left(k+1-m-(q-1)\omega_a \right) \right. \\ & \left. - \Gamma \left(k+1-m-(q-1)\omega_a, \frac{k}{bQ_{ct}^*} \right) \right] - Q_{ct}^{*m} \left[\Gamma(k+1-(q-1)\omega_a) - \Gamma \left(k+1-(q-1)\omega_a, \frac{k}{bQ_{ct}^*} \right) \right] \\ & - k^{m+\alpha} b^{-\alpha} Q_{ct}^{*-\alpha} \left(\Gamma(k+1-m-(q-1)\omega_a - \alpha) - \Gamma \left(k+1-m-(q-1)\omega_a - \alpha, \frac{k}{bQ_{ct}^*} \right) \right) \\ & + k^\alpha b^{-\alpha} Q_{ct}^{*m-\alpha} \left(\Gamma(k+1-(q-1)\omega_a - \alpha) - \Gamma \left(k+1-(q-1)\omega_a - \alpha, \frac{k}{bQ_{ct}^*} \right) \right). \end{aligned} \quad (C1)$$

For the flood-cleaning case ($\alpha < 0$) with $Q_{ct}^* > Q_{cc}^*$ ($b < 1$), we obtain

$$\begin{aligned} \bar{I} = & k_e k_{BL} \left(k_e d \frac{\bar{Q}_s}{\bar{I}} \right)^{q-1/2} \bar{Q}^m S^n \frac{k^{(q-1)\omega_a}}{\Gamma(k+1)} \left[k^m \Gamma(k+1-m-(q-1)\omega_a) \right. \\ & \left. - \Gamma \left(k+1-m-(q-1)\omega_a, \frac{k}{Q_{ct}} \right) \right] - Q_{ct}^{*m} \left[\Gamma(k+1-(q-1)\omega_a) \right. \\ & \left. - \Gamma \left(k+1-(q-1)\omega_a, \frac{k}{Q_{ct}} \right) \right] - k^{m+\alpha} b^{-\alpha} Q_{ct}^{*-\alpha} \left(\Gamma(k+1-m-(q-1)\omega_a - \alpha) \right. \\ & \left. - \Gamma \left(k+1-m-(q-1)\omega_a - \alpha, \frac{k}{Q_{ct}} \right) \right) + k^\alpha b^{-\alpha} Q_{ct}^{*m-\alpha} \left(\Gamma(k+1-(q-1)\omega_a - \alpha) \right. \\ & \left. - \Gamma \left(k+1-(q-1)\omega_a - \alpha, \frac{k}{Q_{ct}} \right) \right). \end{aligned} \quad (C2)$$

For the flood-depositing case ($\alpha > 0$) with $Q_{ct}^* < Q_{cc}^*$ ($b > 1$), we obtain

$$\begin{aligned} \bar{I} = & k_e k_{BL} \left(k_e d \frac{\bar{Q}_s}{\bar{I}} \right)^{\frac{q-1}{2}} \bar{Q}^m S^n \frac{k^{(q-1)\omega_a}}{\Gamma(k+1)} \left[k^m \Gamma \left(k+1-m-(q-1)\omega_a, \frac{k}{bQ_{ct}^*} \right) \right. \\ & \left. - \Gamma \left(k+1-m-(q-1)\omega_a, \frac{k}{Q_{ct}^*} \right) \right] - Q_{ct}^{*m} \left[\Gamma \left(k+1-(q-1)\omega_a, \frac{k}{bQ_{ct}^*} \right) - \Gamma \left(k+1-(q-1)\omega_a, \frac{k}{Q_{ct}^*} \right) \right] \\ & - k^{m+\alpha} b^{-\alpha} Q_{ct}^{*-\alpha} \left(\Gamma \left(k+1-m-(q-1)\omega_a - \alpha, \frac{k}{bQ_{ct}^*} \right) - \Gamma \left(k+1-m-(q-1)\omega_a - \alpha, \frac{k}{Q_{ct}^*} \right) \right) \\ & + k^\alpha b^{-\alpha} Q_{ct}^{*m-\alpha} \left(\Gamma \left(k+1-(q-1)\omega_a - \alpha, \frac{k}{bQ_{ct}^*} \right) - \Gamma \left(k+1-(q-1)\omega_a - \alpha, \frac{k}{Q_{ct}^*} \right) \right). \end{aligned} \quad (C3)$$

Appendix D: Calibrating the Model Using Field Observations of Slope and Width

Channel width and slope as well as drainage area and discharge can be measured in the field with commonly available methods. Under the assumption that the channel is at a long-term steady state, such measurements can be used to calibrate various free parameters in the equations. From Equations 7 and 24, channel width is given by

$$\bar{W} = \left(k_e d \bar{\beta} A \right)^{1/2}. \quad (D1)$$

The slope can be obtained from Equations 12 and 24

$$S = \bar{W}^{-(q/n)} \left(\frac{\bar{\beta} \bar{A} \bar{I}}{F_{Qs} k_{BL}} \right)^{1/n} \bar{Q}^{-(m/n)}. \quad (D2)$$

Finally, Equation 23 gives a further constraint on erodibility k_e in case the long-term incision rate is known.

$$\bar{I} = k_e \frac{\bar{Q}_s}{\bar{W}} \frac{F_I}{F_{Qs}} = k_e \frac{\bar{\beta} \bar{A} \bar{I}}{\bar{W}} \frac{F_I}{F_{Qs}}. \quad (D3)$$

From Equation D3, it follows that

$$k_e = \frac{\bar{W}}{\bar{\beta} A} \frac{F_{Qs}}{F_I}. \quad (D4)$$

With measurements of slope, width, drainage area, mean discharge, and long-term incision rate, and an estimate of the bedload fraction, Equation D2 can be used to calculate k_{BL} . Subsequently, erodibility k_e can be calculated using Equations D4 and D1 can be used to calculate the deflection length scale d .

Appendix E: Upscaling the Stream Power Incision Model

Lague et al. (2005) gave a comprehensive discussion of the upscaled stream power incision model (SPIM). In a stream with variable discharge, the bedrock incision rate according to the SPIM is given by (cf. Lague et al., 2005)

$$I = k_{SPIM} \bar{Q}^{m'} S^{n'} \left(Q^{*m'} - Q_{ce}^{*m'} \right). \quad (E1)$$

The integral is given by

$$\bar{I} = \frac{k^{k+1}}{\Gamma(k+1)} k_{SPIM} \bar{Q}^{m'} S^{n'} \int_{Q_{ce}^*}^{\infty} \exp \left\{ -\frac{k}{Q^*} \right\} \left(Q^{*m'-(2+k)} - Q_{ce}^{*m'} Q^{*-(2+k)} \right) dQ^*. \quad (E2)$$

The long-term incision rate is then given by

$$\bar{I} = \bar{Q}^{m'} S^{n'} \frac{k_{SPIM}}{\Gamma(k+1)} \left[k^{m'} \left(\Gamma(k+1-m') - \Gamma \left(k+1-m', \frac{k}{Q_{ce}^*} \right) \right) - Q_{ce}^{*m'} \left(\Gamma(k+1) - \Gamma \left(k+1, \frac{k}{Q_{ce}^*} \right) \right) \right]. \quad (E3)$$

Notation

Functions

$\exp\{x\}$	Natural exponential function of x .
F_C	Discharge variability-dependent function for the long-term mean bed cover.
F_I	Discharge variability-dependent function for the long-term mean incision rate.
F_{Qs}	Discharge variability-dependent function for the long-term mean sediment transport rate.
$\text{pdf}(Q^*)$	Probability density function of the dimensionless discharge Q^* (Equation 1).
$\Gamma(x)$	Gamma function of x (Equation 2).
$\Gamma(x,c)$	Upper incomplete gamma function of x (Equation 14).

Variables

A	Drainage area [m^2].
A_c	Cross-sectional area of the flow [m^2].
a	Scaling exponent, $C-Q^*$.
B	Scaling exponent, $\beta-A$.
b	Coefficient of proportionality, $Q_{ct}^* \leq Q_{ce}^*$.

C	Fraction of covered bed.
$\langle C \rangle$	Average cover at a given discharge.
\bar{C}	Long-term mean cover.
D	Representative grain size (m).
d	Sideward deflection length scale, reach (m).
g	Acceleration due to gravity (m/s^2).
H	Water depth (m).
I	Instantaneous incision rate (m/s).
\bar{I}	Long-term mean incision rate (m/s).
k	Discharge variability parameter.
k_{bl}	Bedload transport efficiency ($\text{kg m}^{-3m-q}\text{s}^{m-1}$).
k_e	Bedrock erodibility (m^2/s).
k_{SPIM}	Erodibility in stream power model ($\text{m}^{1-3m'}\text{s}^{1-m'}$).
k_s	Steepness index ($\text{m}^{2\theta}$).
K_V	Flow velocity coefficient ($\text{m}^{1-\delta}/\text{s}$).
k_W	Prefactor, downstream hydraulic geometry for width.
$k\beta$	Prefactor in the relationship of and drainage area (m^{-2B}).
k_v	Rock erodibility coefficient.
m	Discharge exponent in bedload equation.
m'	Discharge exponent in the stream power model.
n	Slope exponent in bedload equation.
n'	Slope exponent in the stream power model.
Q	Water discharge (m^3/s).
Q_{max}	Maximum water discharge at which erosion occurs (m^3/s).
Q_{min}	Minimum water discharge at which erosion occurs (m^3/s).
\bar{Q}	Long-term mean water discharge (m^3/s).
Q^*	Dimensionless water discharge, normalized by the long-term mean discharge
Q_{ce}^*	Critical discharge for the onset of erosion in the SPIM (m^3/s).
Q_{ct}^*	Critical discharge for the onset of bedload motion (m^3/s).
Q_{cc}^*	Critical discharge for the change between a fully and partially covered bed (m^3/s).
Q_s	Upstream sediment mass supply (kg/s).
\bar{Q}_s	Long-term mean bedload supply (kg/s).
Q_s	Upstream sediment mass supply (kg/s).
Q_t	Mass sediment transport capacity (kg/s).
q	Width dependence of transport rate, scaling exponent, Q_s-W .
R	Runoff (m/s).
R_h	Hydraulic radius (m).
S	Channel bed slope.
V	Water flow velocity (m/s).
W	Instantaneous channel width [m].
\bar{W}	Channel width at the mean discharge [m].
Y	Young's modulus of the bedrock [$\text{kg m}^{-1}\text{s}^{-2}$].
α	Scaling exponent, $C-Q^*$.
β	Fraction of sediment transported as bedload.
$\bar{\beta}$	Long-term mean of the fraction of sediment transported as bedload.
γ	Dimensionless bedload transport coefficient.
δ	Scaling exponent, flow velocity $V-R_h$.
ρ	Density of water [kg/m^3].
ρ_s	Density of sediment [kg/m^3].
σ_T	Rock tensile strength [$\text{kg m}^{-1}\text{s}^{-2}$].
θ	Concavity index, scaling exponent, $S-A$.
τ	Bed shear stress [N/m^2].
τ^*	Shields stress.
τ_c^*	Critical Shields stress at the onset of bedload motion.

ω_d	Downstream hydraulic geometry exponent for width, scaling exponent $\langle W \rangle - \bar{Q}$
ω_a	At-a-station hydraulic geometry exponent for width, scaling exponent $W - Q^*$

Data Availability Statement

Data were not used, nor created for this research.

Acknowledgments

The author thanks Ron Nativ for discussions and comments on an earlier version of the manuscript. The associate editor and two anonymous reviewers provided valuable comments on a previous version of the manuscript. This study was funded by GFZ. Open access funding enabled and organized by Projekt DEAL.

References

- Attal, M., Cowie, P. A., Whittaker, A. C., Hobley, D., Tucker, G. E., & Roberts, G. P. (2011). Testing fluvial erosion models using the transient response of bedrock rivers to tectonic forcing in the Apennines, Italy. *Journal of Geophysical Research*, 116, F02005. <https://doi.org/10.1029/2010JF001875>
- Auel, C., Albayrak, I., Sumi, T., & Boes, R. M. (2017). Sediment transport in high-speed flows over a fixed bed: 2. Particle impacts and abrasion prediction. *Earth Surface Processes and Landforms*, 42, 1384–1396. <https://doi.org/10.1002/esp.4132>
- Barnhart, K. R., Tucker, G. E., Doty, S. G., Shobe, C. M., Glade, R. C., Rossi, M. W., & Hill, M. C. (2020). Inverting topography for landscape evolution model process representation: 3. Determining parameter ranges for select mature geomorphic transport laws and connecting changes in fluvial erodibility to changes in climate. *Journal of Geophysical Research: Earth Surface*, 125, e2019JF005287. <https://doi.org/10.1029/2019JF005287>
- Beer, A. R., & Turowski, J. M. (2015). Bedload transport controls bedrock erosion under sediment-starved conditions. *Earth Surface Dynamics*, 3, 291–309. <https://doi.org/10.5194/esurf-3-291-2015>
- Beer, A. R., Turowski, J. M., & Kirchner, J. W. (2017). Spatial patterns of erosion in a bedrock gorge. *Journal of Geophysical Research: Earth Surface*, 122, 191–214. <https://doi.org/10.1002/2016JF003850>
- Blom, A., Arkesteijn, L., Chavarrias, V., & Viparelli, E. (2017). The equilibrium alluvial river under variable flow and its channel-forming discharge. *Journal of Geophysical Research: Earth Surface*, 122, 1924–1948. <https://doi.org/10.1029/2017JF004213>
- Bursztyn, N., Pederson, J. L., Tressler, C., Mackley, R. D., & Mitchell, K. J. (2015). Rock strength along a fluvial transect of the Colorado Plateau – Quantifying a fundamental control on geomorphology. *Earth and Planetary Science Letters*, 429, 90–100. <https://doi.org/10.1016/j.epsl.2015.07.042>
- Carson, M. A., & Griffiths, G. A. (1987). Influence of channel width on bed load transport capacity. *Journal of Hydraulic Engineering*, 113(12), 1489–1508. [https://doi.org/10.1061/\(ASCE\)0733-9429\(1987\)113:12\(1489\)](https://doi.org/10.1061/(ASCE)0733-9429(1987)113:12(1489))
- Chatanantavet, P., & Parker, G. (2008). Experimental study of bedrock channel alluviation under varied sediment supply and hydraulic conditions. *Water Resources Research*, 44, W12446. <https://doi.org/10.1029/2007WR006581>
- Cook, K. L., Turowski, J. M., & Hovius, N. (2013). A demonstration of the importance of bedload transport for fluvial bedrock erosion and knickpoint propagation. *Earth Surface Processes and Landforms*, 38, 683–695. <https://doi.org/10.1002/esp.3313>
- Cook, K. L., Turowski, J. M., & Hovius, N. (2020). Width control on event scale deposition and evacuation of sediment in bedrock-confined channels. *Earth Surface Processes and Landforms*, 45(14), 3702–3713. <https://doi.org/10.1002/esp.4993>
- Crave, A., & Davy, P. (2001). A stochastic “precipiton” model for simulating erosion/sedimentation dynamics. *Computers & Geosciences*, 27, 815–827.
- Davy, P., & Lague, D. (2009). Fluvial erosion/transport equation of landscape evolution models revisited. *Journal of Geophysical Research*, 114, F03007. <https://doi.org/10.1029/2008JF001146>
- Deal, E., Braun, J., & Botter, G. (2018). Understanding the role of rainfall and hydrology in determining fluvial erosion efficiency. *Journal of Geophysical Research: Earth Surface*, 123, 744–778. <https://doi.org/10.1002/2017JF004393>
- DiBiase, R. A., & Whipple, K. X. (2011). The influence of erosion thresholds and runoff variability on the relationships among topography, climate, and erosion rate. *Journal of Geophysical Research*, 116, F04036. <https://doi.org/10.1029/2011JF002095>
- Dingle, E. H., Attal, M., & Sinclair, H. D. (2017). Abrasion sets limits on Himalayan gravel flux. *Nature*, 544, 471–474. <https://doi.org/10.1038/nature22039>
- Fernandez Luque, R., & van Beek, R. (1976). Erosion and transport of bed-load sediment. *Journal of Hydraulic Research*, 14, 127–144. <https://doi.org/10.1080/00221687609499677>
- Fernández, R., Parker, G., & Stark, C. P. (2019). Experiments on patterns of alluvial cover and bedrock erosion in a meandering channel. *Earth Surface Dynamics*, 7, 949–968. <https://doi.org/10.5194/esurf-2019-8>
- Finnegan, N. J., Sklar, L. S., & Fuller, T. K. (2007). Interplay of sediment supply, river incision, and channel morphology revealed by the transient evolution of an experimental bedrock channel. *Journal of Geophysical Research*, 112, F03S11. <https://doi.org/10.1029/2006JF000569>
- Foley, M. G. (1980). Bed-rock incision by streams. *The Geological Society of America Bulletin*, 91, 2189–2213.
- Gasparini, N. M., Whipple, K. X., & Bras, R. L. (2007). Predictions of steady state and transient landscape morphology using sediment-flux-dependent river incision models. *Journal of Geophysical Research*, 112, F03S09. <https://doi.org/10.1029/2006JF000567>
- Heritage, G. L., Large, A. R. G., Moon, B. P., & Jewitt, G. (2004). Channel hydraulics and geomorphic effects of an extreme flood event on the Sabie River, South Africa. *Catena*, 58, 151–181. <https://doi.org/10.1016/j.catena.2004.03.004>
- Inoue, T., Izumi, N., Shimizu, Y., & Parker, G. (2014). Interaction among alluvial cover, bed roughness, and incision rate in purely bedrock and alluvial-bedrock channel. *Journal of Geophysical Research: Earth Surface*, 119, 2123–2146. <https://doi.org/10.1002/2014JF003133>
- Johnson, J. P. L., Whipple, K. X., Sklar, L. S., & Hanks, T. C. (2009). Transport slopes, sediment cover, and bedrock channel incision in the Henry Mountains, Utah. *Journal of Geophysical Research*, 114, F02014. <https://doi.org/10.1029/2007JF000862>
- Lague, D. (2010). Reduction of long-term bedrock incision efficiency by short-term alluvial cover intermittency. *Journal of Geophysical Research*, 115, F02011. <https://doi.org/10.1029/2008JF001210>
- Lague, D. (2014). The stream power river incision model: Evidence, theory and beyond. *Earth Surface Processes and Landforms*, 39, 38–61. <https://doi.org/10.1002/esp.3462>
- Lague, D., Hovius, N., & Davy, P. (2005). Discharge, discharge variability, and the bedrock channel profile. *Journal of Geophysical Research*, 110, F04006. <https://doi.org/10.1029/2004JF000259>
- Meyer-Peter, E., & Müller, R. (1948). *Formulas for bedload transport*. Paper presented in 2nd Meeting of International Association of Hydraulic Structures Research, IAHR.

- Mishra, J., & Inoue, T. (2020). Alluvial cover on bedrock channels: Applicability of existing models. *Earth Surface Dynamics*, 8, 695–716. <https://doi.org/10.5194/esurf-8-695-2020>
- Mishra, J., Inoue, T., Shimizu, Y., Sumner, T., & Nelson, J. M. (2018). Consequences of abrading bed load on vertical and lateral bedrock erosion in a curved experimental channel. *Journal of Geophysical Research: Earth Surface*, 123, 3147–3161. <https://doi.org/10.1029/2017JF004387>
- Molnar, P. (2001). Climate change, flooding in arid environments, and erosion rates. *Geology*, 29, 1071–1074. [https://doi.org/10.1130/0091-7613\(2001\)029<1071:CCFIAE>2.0](https://doi.org/10.1130/0091-7613(2001)029<1071:CCFIAE>2.0)
- Molnar, P., Anderson, R. S., Kier, G., & Rose, J. (2006). Relationships among probability distributions of stream discharges in floods, climate, bed load transport, and river incision. *Journal of Geophysical Research*, 111, F02001. <https://doi.org/10.1029/2005JF000310>
- Rickenmann, D. (2001). Comparison of bed load transport in torrent and gravel bed streams. *Water Resources Research*, 37, 3295–3305. <https://doi.org/10.1029/2001WR000319>
- Scherler, D., DiBiase, R. A., Fisher, G. B., & Avouac, J.-P. (2017). Testing monsoonal controls bedrock river incision in the Himalaya and eastern Tibet with a stochastic-threshold stream power model. *Journal of Geophysical Research: Earth Surface*, 122, 1389–1429. <https://doi.org/10.1002/2016JF004011>
- Seidl, M. A., & Dietrich, W. E. (1992). The problem of channel erosion into bedrock. *Catena Supplement*, 23, 101–124.
- Shepherd, R. G. (1972). Incised river meanders: Evolution in simulated bedrock. *Science*, 178(4059), 409–411. <https://doi.org/10.1126/science.178.4059.409>
- Sklar, L. S., & Dietrich, W. E. (2001). Sediment and rock strength controls on river incision into bedrock. *Geology*, 29, 1087–1090. [https://doi.org/10.1130/0091-7613\(2001\)029<1087:SARSCO>2.0.CO;2](https://doi.org/10.1130/0091-7613(2001)029<1087:SARSCO>2.0.CO;2)
- Sklar, L. S., & Dietrich, W. E. (2004). A mechanistic model for river incision into bedrock by saltating bed load. *Water Resources Research*, 40, W06301. <https://doi.org/10.1029/2003WR002496>
- Sklar, L. S., & Dietrich, W. E. (2006). The role of sediment in controlling steady state bedrock channel slope: Implications of the saltation-abrasion incision model. *Geomorphology*, 82, 58–83. <https://doi.org/10.1016/j.geomorph.2005.08.019>
- Smith, T. R., & Bretherton, F. P. (1972). Stability and the conservation of mass in drainage basin evolution. *Water Resources Research*, 8, 1506–1529.
- Tomkin, J. H., Brandon, M. T., Pazzaglia, F. J., Barbour, J. R., & Willett, S. D. (2003). Quantitative testing of bedrock incision models for the Clearwater River, NW Washington state. *Journal of Geophysical Research*, 108(B6), 2308. <https://doi.org/10.1029/2001JB000862>
- Tucker, G. E. (2004). Drainage basin sensitivity to tectonic and climatic forcing: Implications of a stochastic model for the role of entrainment and erosion thresholds. *Earth Surface Processes and Landforms*, 29, 185–205. <https://doi.org/10.1002/esp.1020>
- Turowski, J. M. (2010). Probability distributions of bedload transport rates: A new derivation and comparison with field data. *Water Resources Research*, 46, W08501. <https://doi.org/10.1029/2009WR008488>
- Turowski, J. M. (2018). Alluvial cover controlling the width, slope and sinuosity of bedrock channels. *Earth Surface Dynamics*, 6, 29–48. <https://doi.org/10.5194/esurf-6-29-2018>
- Turowski, J. M. (2020). Mass balance, grade, and adjustment timescales in bedrock channels. *Earth Surface Dynamics*, 8, 103–122. <https://doi.org/10.5194/esurf-8-103-2020>
- Turowski, J. M., Badoux, A., Leuzinger, J., & Hegglin, R. (2013). Large floods, alluvial overprint, and bedrock erosion. *Earth Surface Processes and Landforms*, 38, 947–958. <https://doi.org/10.1002/esp.3341>
- Turowski, J. M., & Hodge, R. A. (2017). A probabilistic framework for the cover effect in bedrock erosion. *Earth Surface Dynamics*, 5, 311–330. <https://doi.org/10.5194/esurf-5-311-2017>
- Turowski, J. M., Hovius, N., Hsieh, M.-L., Lague, D., & Chen, M.-C. (2008). Distribution of erosion across bedrock channels. *Earth Surface Processes and Landforms*, 33, 353–363. <https://doi.org/10.1002/esp.1559>
- Turowski, J. M., Hovius, N., Wilson, A., & Horng, M.-J. (2008). Hydraulic geometry, river sediment and the definition of bedrock channels. *Geomorphology*, 99(1–4), 26–38. <https://doi.org/10.1016/j.geomorph.2007.10.001>
- Turowski, J. M., Lague, D., & Hovius, N. (2007). Cover effect in bedrock abrasion: A new derivation and its implication for the modeling of bedrock channel morphology. *Journal of Geophysical Research*, 112, F04006. <https://doi.org/10.1029/2006JF000697>
- Valla, P., van der Beek, P., & Lague, D. (2010). Fluvial incision into bedrock: Insights from morphometric analysis and numerical modeling of gorges incising glacial hanging valleys (western Alps, France). *Journal of Geophysical Research*, 115(F2), F02010. <https://doi.org/10.1029/2008JF001079>
- van der Beek, P., & Bishop, P. (2003). Cenozoic river profile development in the upper Lachlan catchment (SE Australia) as a test of quantitative fluvial incision models. *Journal of Geophysical Research*, 108(B6), 2309. <https://doi.org/10.1029/2002JB002125>
- Venditti, J. G., Li, T., Deal, E., Dingle, E., & Church, M. (2020). Struggles with stream power: Connecting theory across scales. *Geomorphology*, 366, 106817. <https://doi.org/10.1016/j.geomorph.2019.07.004>
- Whipple, K. X. (2004). Bedrock rivers and the geomorphology of active orogens. *Annual Review of Earth and Planetary Sciences*, 32, 151–185. <https://doi.org/10.1146/annurev.earth.32.101802.120356>
- Whipple, K. X., & Tucker, G. E. (2002). Implications of sediment-flux-dependent river incision models for landscape evolution. *Journal of Geophysical Research*, 107(B2), 2039. <https://doi.org/10.1029/2000JB000044>
- Whitbread, K., Jansen, J., Bishop, P., & Attal, M. (2015). Substrate, sediment, and slope controls on bedrock channel geometry in postglacial streams. *Journal of Geophysical Research: Earth Surface*, 120, 779–798. <https://doi.org/10.1002/2014JF003295>
- Wobus, C., Whipple, K. X., Kirby, E., Snyder, N., Johnson, J., Spyropoulou, K., et al., (2006). Tectonics from topography: procedures, promise, and pitfalls. In S. D. Willett N. Hovius M. T. Brandon & D. Fisher (Eds.) *Geological Society of America Special Paper 398*, (pp. 55–74). Washington, DC: Geological Society of America. [https://doi.org/10.1130/2006.2398\(04\)](https://doi.org/10.1130/2006.2398(04))
- Wohl, E., & Ikeda, H. (1997). Experimental simulation of channel incision into a cohesive substrate at varying gradients. *Geology*, 25, 295–298. [https://doi.org/10.1130/0091-7613\(1997\)025<0295:ESOCII>2.3.CO;2](https://doi.org/10.1130/0091-7613(1997)025<0295:ESOCII>2.3.CO;2)
- Zhang, L., Parker, G., Stark, C. P., Inoue, T., Viparelli, E., Fu, X., & Izumi, N. (2015). Macro-roughness model of bedrock-alluvial river morphodynamics. *Earth Surface Dynamics*, 3, 113–138. <https://doi.org/10.5194/esurf-3-113-2015>